

Chapter III

Head-to-Tail Interlocking Aromatic Rings of a Hydrazine Functionalized Schiff Base for the development of Nano-aggregates with blue emission: Structural and Spectroscopic Characteristics

3.1. Introduction

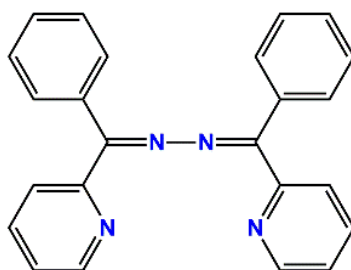
The advancement of functional luminophores in light-emitting and light-harvesting processes shows a great promise in bringing novel characteristics and properties to the materials.^[1,2] The evolution of light-dependent molecular devices and technologies is triggered a paramount interest to material scientists for the indispensable contribution of molecular devices in scientific and societal advancement.^[3] In this context, molecular aggregation beyond the microscopic level is a highly fascinating phenomenon that attributes novel properties to functional materials and the design of high-tech photo-electronic devices.^[4-6] Nowadays, the aggregation-induced emission (AIE) phenomenon provides an exciting avenue in scientific research to unveil the properties of molecular aggregate.^[1-3] The advent of newly developed properties endow by molecular aggregates introduce new characteristics and functionalities in the molecular aggregate compared to single molecules.^[3,4,7]

AIE deals with a class of molecules is dim or low emission properties in dilute solution. However, the compounds display a pronounced effect on enhancing emission properties in molecular aggregates.^[8] A systematic study by Tang *et al.* on different AIE systems summarises that the restriction of active intramolecular motion in the molecular aggregate limits the excited-state non-radiative decay. In contrast, dynamic intramolecular motion increases the non-radiative decay and quenches the molecular emission.^[9] Further, the motion-responsive molecular aggregates exhibits strong emission properties in solid state, enabling unique applications in different dimensions, including chemical sensors, fluorescent imaging, photonic drugs, bio-probes, optoelectronics and others.^[4-7,10]

Typically, azines contain aromatic units bridged through rotatable N–N bonds and were the highly stable condensation products of carbonyl compounds and hydrazine.^[14,15] Azine compounds show an excellent promise for their straightforward synthetic approach, high yield and easy isolation of the products, cost-effective, high stability to applied for suitable technological applications and devices.^[11-13] In general,

H-type aggregation induces a non-radiative deactivation process, while the J-type aggregation imparts a relatively high fluorescence efficiency.^[17,18]

Intermolecular non-covalent interactions involving aromatic systems are considered emerging inductors to develop a vast array of long-range crystalline architectures through crystal engineering.^[19-22] Different weak forces such as hydrogen bonding, $\pi \cdots \pi$ and C-H $\cdots\pi$ short contacts in crystalline materials are imperative to design new materials with novel properties.^[23,24] Therefore, the proper understanding of weak forces allows envisioning the role of supramolecular assemblies in developing novel functional properties.^[25,26] It is evident that weak intermolecular forces have a pronounced effect on AIE property and, eventually, may brought a substantial change in the size and phase of crystalline materials.^[27,28] Herein, I have designed and synthesized of an azine type Schiff base and explored its aggregation behaviour with a suite of spectroscopic and crystallographic studies. The dominant dispersive forces significantly stabilize the cluster of molecules and mingle the aromatic rings through the head to tail type interlocking. This phenomenon imposes a strict restriction on the intramolecular rotation and vibration of aromatic rings in the Schiff base with the development of blue emission. [L^2 = 1,2-bis(phenyl(pyridin-2-yl)methylene)hydrazine, **Scheme 3.1**]



Scheme 3.1. Schematic diagram of the ligand L^2

3.2. Experimental

3.2.1. Preparation of the complex

3.2.1.1 Chemicals, solvents and starting materials

>99% pure 2-benzoylpyridine (Aldrich, USA) and >98% pure hydrazine monohydrate (TCI, Japan) was procured from the respective commercial sources. All the chemicals and solvents were of spectroscopic grade and used as received.

3.2.1.2. General procedure for the synthesis of Schiff base

The Schiff base was prepared following a reported synthetic procedure with a little modifications.^[29-32] The Schiff base was synthesised by refluxing 2-benzoylpyridine (0.3660 g, 2mmol) with hydrazine monohydrate (0.050 g, 1 mmol) in 30 ml ethanol for 10h. The reaction solution was filtered and dried. The compound was stored *in vacuo* over CaCl₂. Yield: 0.360 g (~86.50%).

3.2.2. Physical measurements

The infrared spectrum of the compound was recorded with an FTIR-8400S SHIMADZU spectrophotometer in the range 400-3600 cm⁻¹. The ¹H and ¹³C NMR spectra of L² were obtained on a Bruker Advance 400 MHz spectrometer at 25 °C. The MALDI TOF mass spectrum of the Schiff base was recorded using a Q-tof-micro quadruple mass spectrometer. All the ground-state absorption spectra were recorded on a JASCO V-730 UV-Vis spectrophotometer, and the fluorescence spectra were measured on a Hitachi F-7000 spectrofluorometer. Elemental analyses were carried out on a Perkin Elmer 2400 CHN microanalyser.

Table 3.1. Elemental analysis of L²

Compound (Mol formula)	Found (Calcd)%		
	C	H	N
L ² (C ₂₄ H ₁₈ N ₄)	79.58 (79.54)	5.05 (5.01)	15.50 (15.46)

3.2.3. Crystal structure determination, refinement and Hirshfeld surface analysis

The Schiff base's single crystal X-ray diffraction data were collected on a Rigaku XtaLABmini diffractometer equipped with Mercury 375R (2×2 bin mode) CCD detector. The data were collected with graphite monochromated Mo-K α radiation ($\lambda=0.71073$ Å) at 100 K using ω scans. The data were reduced using CrysAlisPro 1.171.39.35c^[33], and the space group determination was done using Olex2. The structure is resolved by the dual space method using SHELXT-2015 and refined by full-matrix least-squares procedures using the SHELXL-2015^[34,35] software package through the OLEX2 suite.^[36] The Crystal Explorer17.5^[37] programme was used to generate Hirshfeld surfaces and 2D fingerprint plots of the Schiff base. The details of the analysis are reported elsewhere.^[38,39]

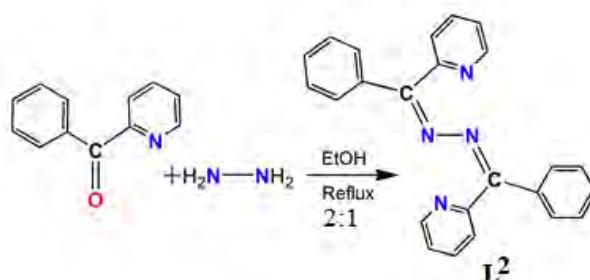
3.2.4. Preparation and characterisation of the molecular aggregate

A stock solution of 1.020 mM L^2 was prepared in a DMSO medium. 20 μ L of the DMSO solution of L^2 was injected into 2 mL of Milli-Q-water and kept undisturbed for 10 mins at room temperature. The molecular aggregate of L^2 was developed following the drop-casting method and recorded the Field Emission Scanning Electron Microscope (FESEM) images on a clean aluminium foil. FESEM images and the electron dispersive X-ray (EDX) plot were recorded with a JSM-6700F FESEM, JEOL, Japan instrument, which confirmed the nature of molecular aggregate in the solid state. The dynamic light scattering (DLS) study of the aggregation studied in an aqueous medium was carried out at 25 $^{\circ}$ C on a Malvern Instrument with Zetasizer Nano ZS90 instrument. The hydrodynamic size of the L^2 was measured by adding 100 μ L of L^2 solution to 1.5 mL of water and recorded in triplicate to find an average number size distribution.

3.3. Results and discussion

3.3.1. Synthesis and formulation

The Schiff base, L^2 was synthesized through the condensation reaction between hydrazine and 2-benzoyl pyridine in ethanol and under refluxing condition for 8h. The colourless crystalline products were developed through the method of recrystallization in methanol.



Scheme 3.2. Synthetic route of L^2

3.3.2. Infrared spectral analysis

The FT-IR spectrum of the Schiff base showed the characteristic stretching vibrations (Fig. 3.1) at 1624 and 1582 cm^{-1} which were assignable to the azomethine group of the Schiff base. Other peaks at 1460 and 1349 cm^{-1} for L^2 were attributed to $-C=C-$ groups in the Schiff base. These appearances of the characteristic peaks resembled very well

with the previously reported values.^[40,41] The infrared spectral data are given below **Table 3.2.**

Table 3.2. Infrared spectral data^a of **L²**

Compound	ν (cm ⁻¹)	Functional Group
L²	1624, 1582	-C=N-
	1460, 1349	-C=C-

^aKBr disc.

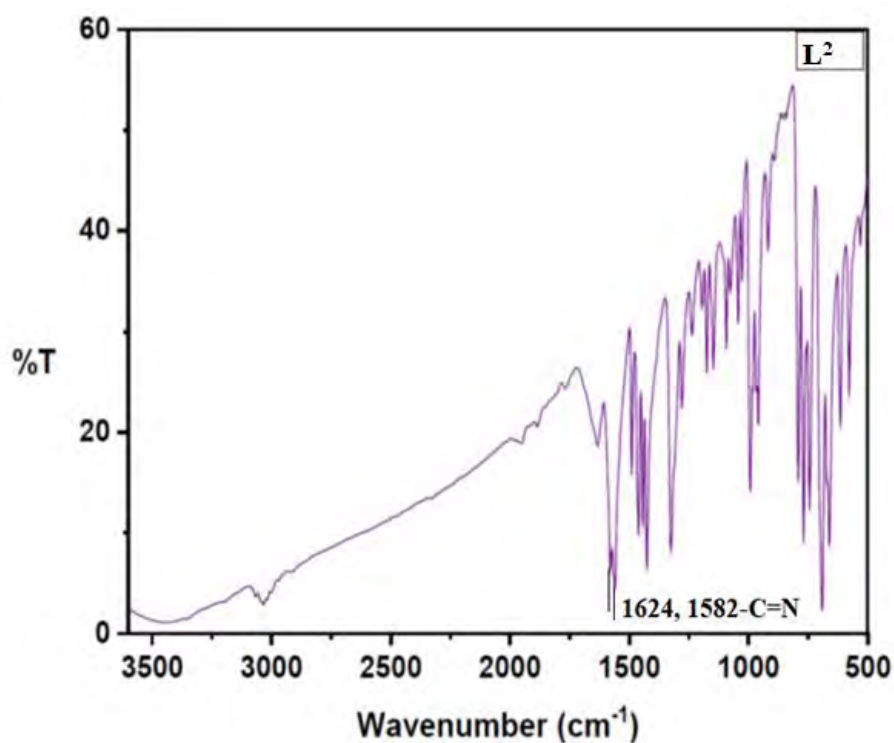


Fig. 3.1. IR spectrum of **L²**

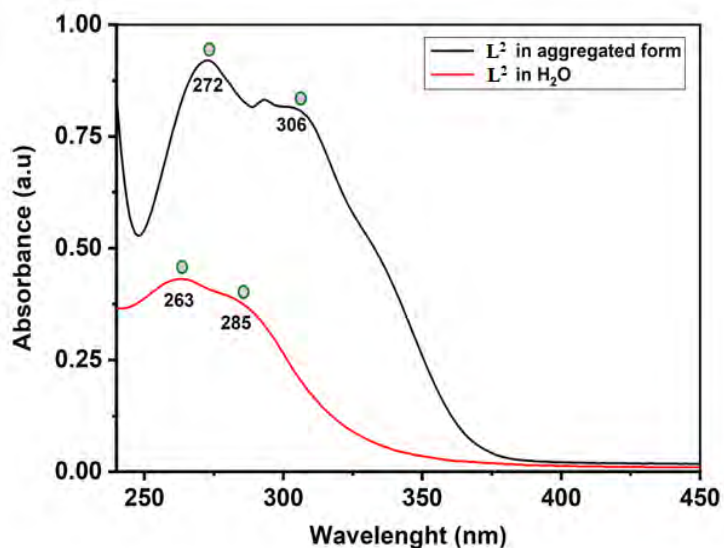
3.3.3. Electronic spectral analysis

The electronic spectrum of **L²** was recorded in aqueous and DMSO media in the 200-900 nm range. The electronic spectrum of **L²** in DMSO showed blue-shifted electronic bands than those in the aqueous solution. **L²** exhibited characteristic absorption bands at 263 and 285 nm (**Fig. 3.2.**), attributing the intra-ligand $\pi-\pi^*/n-\pi^*$ electronic transitions of the **L²** probe. The reported electronic bands for **L²** were in well-agreement with the reported values.^[43]

Table 3.3. UV-Vis data of L^2

Compound	λ_{max} , nm
L^2	263(0.44), 285(0.35)

^aaqueous-DMSO medium at 298K

**Fig. 3.2.** UV-Vis spectra of L^2 and aggregated form of L^2

3.3.4. Fluorescence spectral analysis

The steady-state fluorescence spectrum of L^2 in an aqueous medium was also recorded and shown in **Fig. 3.3**. The emission maximum for L^2 was observed at 300 nm with low intensity. The nature of the fluorescence spectrum suggests its mild fluorescence properties in the aqueous medium at room temperature.

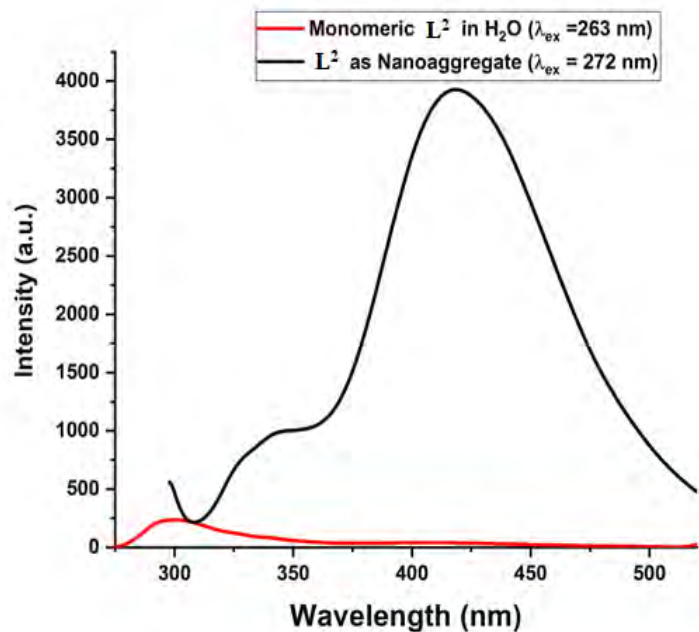


Fig. 3.3. Steady-state fluorescence spectra of the monomeric form and aggregated form of L² in aqueous phase at room temperature

3.3.5. NMR spectral analysis

The NMR spectral analysis of L² was carried out in DMSO-d₆. **Fig. 3.4** and **3.5** displayed the ¹H and ¹³C NMR spectra of L², respectively. The appearance of the proton's signals in the range 8.70 to 6.61 ppm corresponded to the aromatic-H of phenyl and pyridine rings for L² (**Fig. 3.4**). The characteristic C-signals of L² were observed from 159.64 to 121.11 ppm in the ¹³C NMR spectra (**Fig. 3.5**) which confirmed the presence of azomethine-C and aromatic-C atoms. The dense-splitting patterns of the signals were attributed to the presence of Ar-H and Ar-C in L² and portrayed a pure signature for the existence of non-covalent interactions as previously evident from the report of Zhao et al.^[42]

3.3.6. MALDI TOF Mass spectral analysis

The MALDI TOF mass spectrum was also recorded for L^2 at room temperature, which confirmed the presence of molecular ion peak at m/z 362.4837 (Fig. 3.6). The absence of any other peaks in the mass spectrum ensured the absence of the impurities in the solution.

Table 3.4. MALDI TOF mass spectral data^c of L^2

Compound	Molecular ion peak (m/z) (Calc.)
L^2	362.4837 (362.15)

^caqueous-DMSO solution at 298K

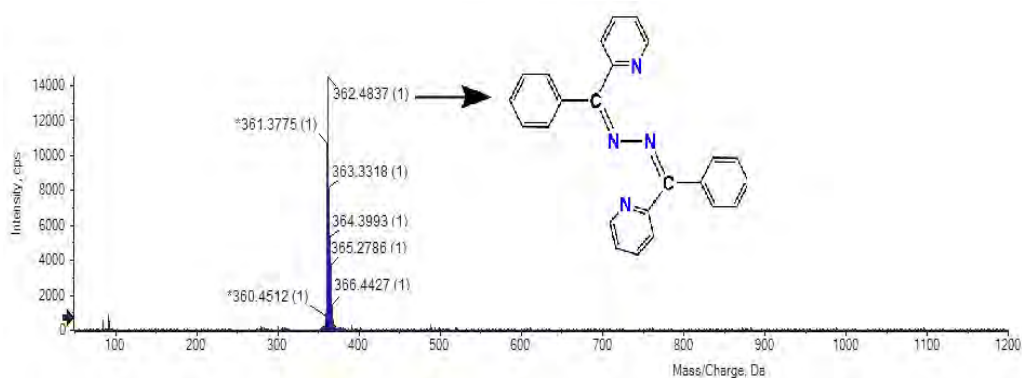


Fig. 3.6. MALDI TOF Mass plot of L^2

3.3.7. Microscopic analysis of the aggregate of L^2

In order to study the aggregation properties of the molecular form of L^2 in solution phase, the FESEM images of the aggregated form of L^2 (Fig. 3.7 a.) were recorded at room temperature. The individual particles of L^2 probe in the aggregated form were observed well rectangular shaped. FESEM images exhibit a large number of aggregated islands of the monomeric L^2 particles in solid state. Very interestingly, the L^2 particles in each of the aggregated islands get agglomerated with each other in solid state. Close inspection on the nature of agglomeration suggested that most of the individual particles participated in fusion with others using different edges of the rectangular shaped particle. It is better to say strong head-to-tail interlocking of individual particles were observed through the edges of rectangular particles in the aggregated form. The average size of the individual particles was determined as ~ 250 nm from the FESEM images. Furthermore, EDX spectral characterization with elemental mapping was used to determine the purity of the aggregated form (Fig. 3.7b). EDX spectrum showed a perfect elemental distribution of L^2 in the aggregated form. Absence of any other

elements in the spectrum suggested that its absolute purity in the aggregated form. Elemental mapping for L^2 further consolidates the purity of the nano-aggregates (**Fig. 3.7c**). Moreover, the size of the aggregated form of L^2 was determined with dynamic light scattering (DLS) measurements (**Fig. 3.8**). The DLS plot of L^2 in aqueous phase indicated the average size of individual particles in the aggregated form is 270 nm. The effect of the solution concentration on the aggregation behaviour of L^2 was also investigated. For L^2 , the particle size was increased with the increase of the concentration of monomer L^2 in solution phase.

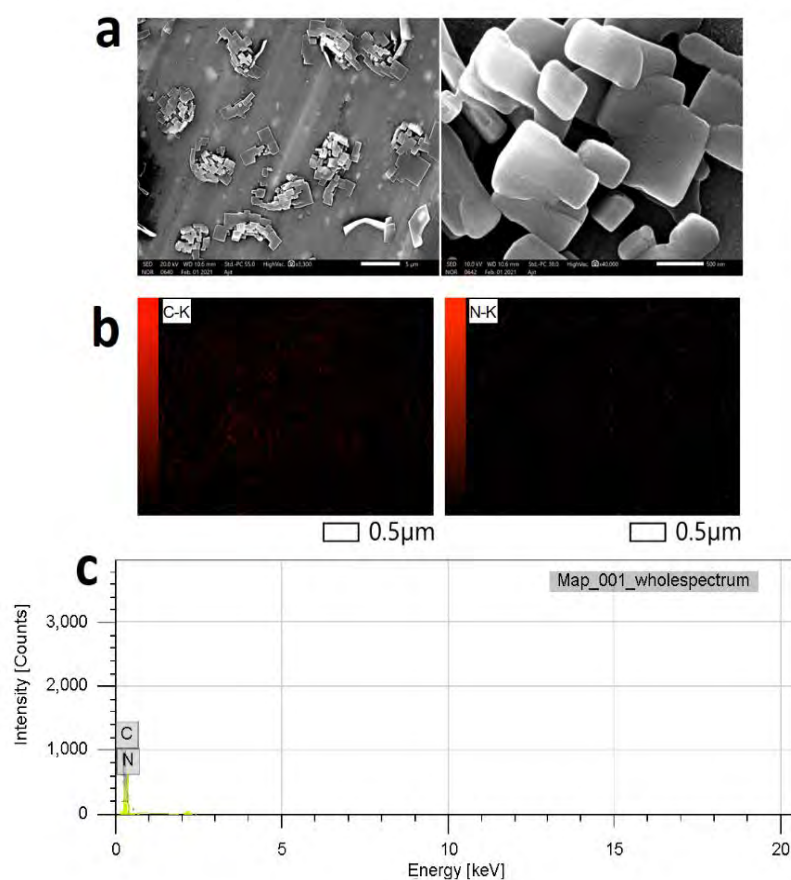


Fig. 3.7. a) FESEM images for the aggregated form of L^2 ; b) Elemental mapping of the molecular aggregate of L^2 ; c) EDX plot showing the distributed % of C and N in the aggregated form

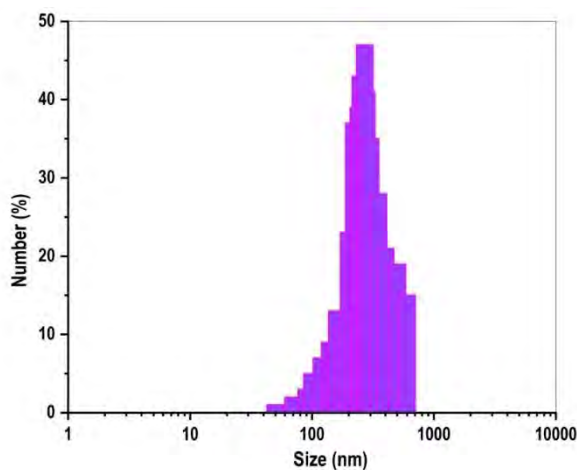


Fig. 3.8. Dynamic light scattering measurement of L^2 in the aggregated form in aqueous médium

3.3.8. Spectroscopic studies on the L^2 aggregate

The insight of the molecular aggregation and the nano-aggregates' photophysical properties were investigated in detail. **Fig. 3.2** showed the comparison of the spectral bands of L^2 and its aggregated form, respectively. It is well observed from **Fig. 3.2** that the absorption spectral profile of L^2 aggregates (272 and 306 nm) is red-shifted compared to the monomeric form of L^2 (263 and 285 nm) in the aqueous phase. Literature on molecular aggregation suggests that a red-shift of the electronic band for a species commonly happened for the J type of aggregation.^[17,18] In this case, an average red-shift of ~10-20 nm was noticed for the absorption bands of the L^2 aggregates compared to its monomeric form, and this phenomenon was a pure indication for the development of J aggregates in the aqueous phase.

To consolidate the origin of the red-shift in the aggregated form of L^2 and found the solvent role, the polarity of the solvent was varied. The absorbance of L^2 was measured in another polar system (methanol: water), where the polarity of the solvent mixture was kept close to that of water: DMSO solvent mixture. The absorption maxima of L^2 in the methanol: water mixture found at 261 nm that was lower than the wavelength maximum (272 nm) of L^2 aggregates. The larger red-shift of the electronic band for L^2 nano-aggregates confirmed that the solvent polarity didn't induce this red-shift of the electronic band; perhaps the structural aggregation remained the driving force for the L^2 aggregation. The molecular exciton theory was explained the shifts in the electronic band of the aggregated forms.^[44] By the principle of molecular exciton theory, a

molecule was treated as a point dipole, and the excitonic energy state of the molecular aggregate was splitted into two tiers based on the nature of dipoles.^[45,46] The resultant electronic transition was proceeded through lower or higher energy transitions leading to J and H type of molecular aggregation. The different kinds of dipole-dipole interactions within two monomers in the aggregated form were principally accountable for splitting energy levels in the molecular aggregates.^[45,46]

The molecular exciton theory further suggested that face-to-face interactions of the transition dipoles for H-aggregates make a shift of absorption maximum towards the blue region while a head-to-tail type of orientations for J-aggregates makes a shift in absorption maximum to the red region. Crystal structure analysis and detailed studied on self-assembly of L^2 provided an essential source of light on this aspect. The excited states of these aggregates were also investigated with the measurement of steady-state and time-resolved fluorescence studied. **Fig. 3.3** displays the comparison of the fluorescence spectra of L^2 in its monomeric with the aggregated forms under identical parameter set up.

It was evident from **Fig. 3.3** that upon excitation on 272 nm, the emission maxima for the L^2 nano-aggregate was red-shifted than its monomeric form. The fluorescence intensity of the L^2 nano-aggregate enhanced by ~20 fold in intensity with the emission of blue light. Therefore, upon aggregation, the mildly fluorescent monomeric L^2 turns out to be highly fluorescent with blue light emission. The measurement of an average lifetime in the aqueous phase, estimated as $t = 0.99$ ns (**Fig. 3.9**) further confirmed the highly emissive characteristics of the nano-aggregate. The excited states of the nano-aggregate get stabilised upon interlocking of the aromatic rings for L^2 in the aqueous medium and exhibited intense blue light emission.

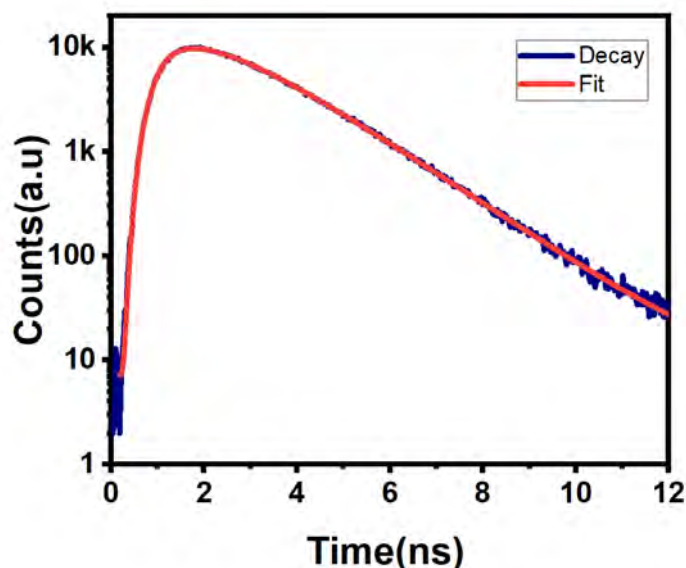


Fig. 3.9. Time-dependent photoluminescence decay profile for L^2 in aggregated form

3.3.9. X-ray crystallographic analysis and self-assembly

The refinement parameters of crystallographic data and structure of the L^2 are given in **Table 3.5**. The single crystals of L^2 were successfully grown in solution to reveal the nature of weak intermolecular forces in the development of nano-aggregate. The crystal structure analysis revealed that the molecule crystallised in a monoclinic crystal system. The ball and stick model of the asymmetric unit and molecular structure of the Schiff base is shown in **Fig. 3.10a** and **Fig. 3.10b**. The structural refinement parameters are summarised in **Table 3.5**. The bond distances and bond angles of the compound are presented in **Table 3.5**. The Schiff base crystallised in a nearly planar *anti*-stereomer as revealed by the bond angles' measurement (**Fig 3.10d**, **Table 3.6**). The C6-N2 and N2–N2a bonds corresponded to a pure double and single bond character, as evident from their bond distance values, 1.295(\pm 0.0017) Å and 1.3888 (\pm 0.0015) Å, respectively (**Table 3.6**).

Table 3.5. Crystallographic data of L^2

Parameters	L^2
CCDC Number	1275289
Empirical formula	$C_{24}H_{18}N_4$
Formula weight	362.42
Temperature (K)	100
Crystal system	Monoclinic
Space group	$C2/c$
a (Å)	21.6921(9)
b (Å)	5.5760(2)

c (Å)	15.2461(5)
Volume (Å ³)	1840.79(12)
Z	4
ρ (gcm ⁻³)	1.308
μ (mm ⁻¹)	0.079
F (000)	760
θ ranges (°)	2.7-32.8
R(int)	0.030
Number of unique reflections	3208
Total number of reflections	10872
Final R indices	0.0668, 0.2199
Largest peak and hole (eÅ ⁻³)	0.58, -0.50

Weighting Scheme: $R = \frac{\sum |F_o| - |F_c|}{\sum |F_o|}$, $wR2 = \left[\frac{\sum w(F_o^2 - F_c^2)^2}{\sum w(F_o^2)^2} \right]^{1/2}$, Calc. $w = \frac{1}{[\sigma^2(F_o^2) + (0.1158P)^2 + 1.4557P]} (L^2)$; where $P = (F_o^2 + 2F_c^2)/3$.

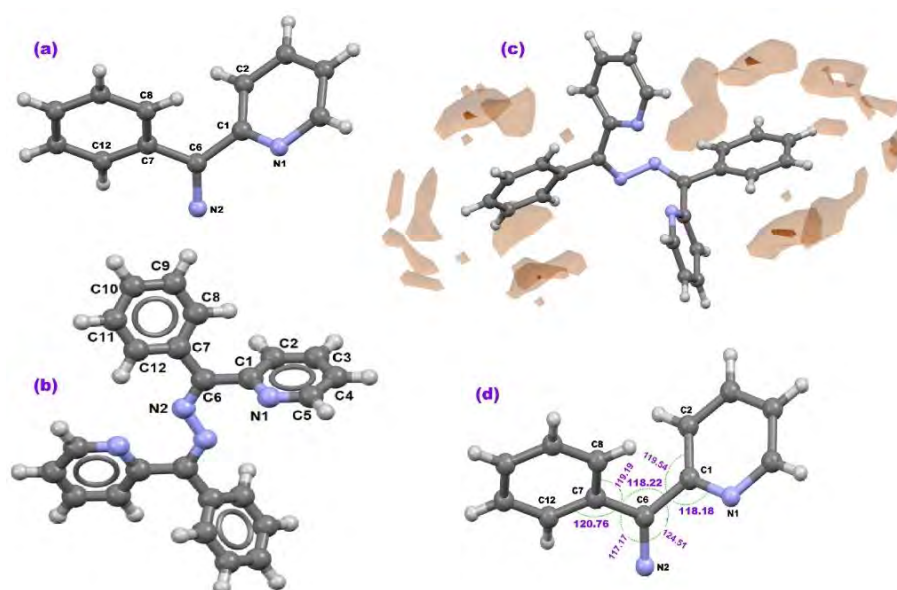


Fig. 3.10. Displacement ellipsoid representation of the molecule: (a) Asymmetric unit of the Schiff base; (b) Ball and stick model of the compound; (c) Interaction propensity of the molecule; (d) Planarity of the asymmetric unit

Table 3.6. Selected bond distances (Å) and angles (°) for the Schiff base of **L**²

Bond distances(Å)			
N1–C1	1.3682(0.0017)	C4–C5	1.3880(0.0020)
N1–C5	1.3680(0.0020)	C6–C7	1.4810(0.0020)
N2–C6	1.2954(0.0017)	C7–C8	1.3850(0.0020)
N2–N2_a	1.3888(0.0015)	C7–C12	1.4060(0.0020)
C1–C2	1.3810(0.0020)	C8–C9	1.3870(0.0020)
C1–C6	1.4954(0.0018)	C9–C10	1.3890(0.0020)
C2–C3	1.3830(0.0020)	C10–C11	1.3960(0.0020)
C3–C4	1.3880(0.0020)	C11–C12	1.3850(0.0020)
Bond angles(°)			
C1–N1–C5	118.49(0.13)	C3–C4–C5	118.87(0.14)
N2_a–N2–C6	116.90(0.11)	C1–C6–C7	118.22(0.11)
N1–C1–C2	122.24(0.13)	C6–C7–C8	119.19(0.13)
N1–C1–C6	118.17(0.12)	C6–C7–C12	120.76(0.13)
N1–C5–C4	121.45(0.15)	C8–C7–C12	120.04(0.14)
N2–C6–C1	124.51(0.12)	C7–C8–C9	119.73(0.15)
N2–C6–C7	117.17(0.11)	C8–C9–C10	120.86(0.16)
C2–C1–C6	119.54(0.11)	C9–C10–C11	119.39(0.16)
C1–C2–C3	118.59(0.14)	C10–C11–C12	120.28(0.15)
C2–C3–C4	120.34(0.14)	C7–C12–C11	119.70(0.15)

The packing diagram of the Schiff base showed edge to face type orientations of the asymmetric units along the *b* axis (**Fig. 3.11**). There was no considerable intermolecular H-bonding in the self-assembled structure. However, long distant $\pi\cdots\pi$ and short-ranged C–H $\cdots\pi$ interactions played a significant role in forming self-assembled crystalline architecture. Interaction mapping over the molecule further suggested the high propensity of the hydrophobic interaction (**Fig. 3.10C**). In the structure of **L**², four aromatic rings (two pyridine and two phenyl rings) were connected to imine-Cs through N–N single bonds in this molecule. Close inspection on the supramolecular framework (**Fig. 3.12**) suggests that the pyridine centroids stacked through a weaker $\pi\cdots\pi$ interactions, while the phenyl centroids exhibited short-ranged C–H $\cdots\pi$ interactions in the crystalline phase (**Table 3.7**).^[47,48]

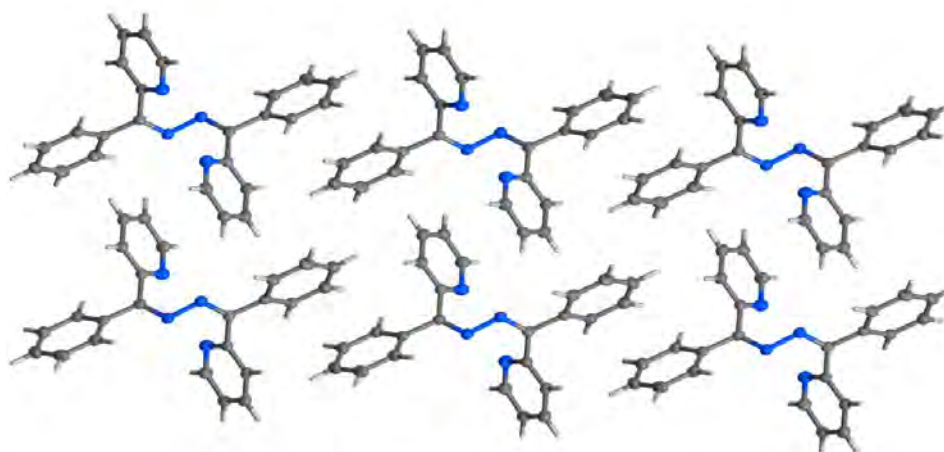


Fig. 3.11. Molecular packing of L^2 along ac plane

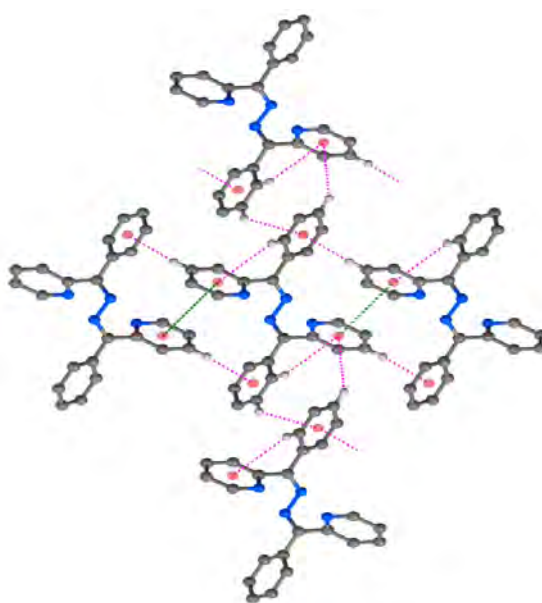


Fig. 3.12. Development of long-range crystalline architecture of L^2 mediated by C–H $\cdots\pi$ and $\pi\cdots\pi$ interactions

Table 3.7. C–H $\cdots\pi$ and $\pi\cdots\pi$ Interaction parameter (\AA , $^\circ$) for L^2

$\pi\cdots\pi$ Interaction (\AA , $^\circ$) for L^2

Cg...Cg	Cg-Cg distance (\AA)	Symmetry code
Cg(1)- Cg(1)	3.86	1-X,1-Y,1-Z

C–H $\cdots\pi$ Interactions (\AA , $^\circ$) for L^2

X–H...Cg	H..Cg (\AA)	X...Cg (\AA)	$\angle\text{XHCg}(^\circ)$	Symmetry code
C(9)–H(9)....Cg(2)	2.94	3.578(17)	126	1/2-X,-1/2+Y,1/2-Z
C(3)–H(3)...Cg(2)	3.18	3.807	124.9	-

3.3.10. Hirshfeld surface and energy framework analysis

The Hirshfeld surface analysis was further carried out to understand the role of intermolecular interactions, as illustrated in **Fig. 3.13**. The surface volume and surface area of L^2 were calculated as 451.84 \AA^3 and 411.11 \AA^2 , with asphericity and globularity indices evaluated as 0.094 and 0.693, respectively. The intermolecular interactions of L^2 were also manifested in terms of two-dimensional fingerprint plots between d_e and d_i (**Fig. 3.14**). The highly influential C–H \cdots π interaction contributes nearly 31.5% of total Hirshfeld surface coverage was a nearly sharp tooth in fingerprint plots which indicated the strength of interaction. The $\pi\cdots\pi$ interaction has only about 3% of Hirshfeld surface coverage and the bright blue spot-on fingerprint plot represented the strength of the interaction. The absence of any sharp tooth from fingerprint plots indicated the lack of any strong hydrogen bonding interactions in the molecule, i.e. less contribution from the Coulomb energy parameter in total energy expression. One centroid of an electron-deficient pyridyl moiety attracts two C–H protons of electron-dense benzene ring forming C–H(donor) \cdots π (acceptor) interaction where electron density of electron-deficient pyridyl moiety was increased to some extent over the other electron-deficient pyridyl ring (oriented in head-to-tail fashion) which bearded a single C–H(donor) \cdots π (acceptor) interaction. The C–H \cdots π and $\pi\cdots\pi$ interactions were the only interactions involved in developing long-range supramolecular crystal architecture. The percentage share of individual elements with other elements for crystalline architecture presented in **Table 3.8**.

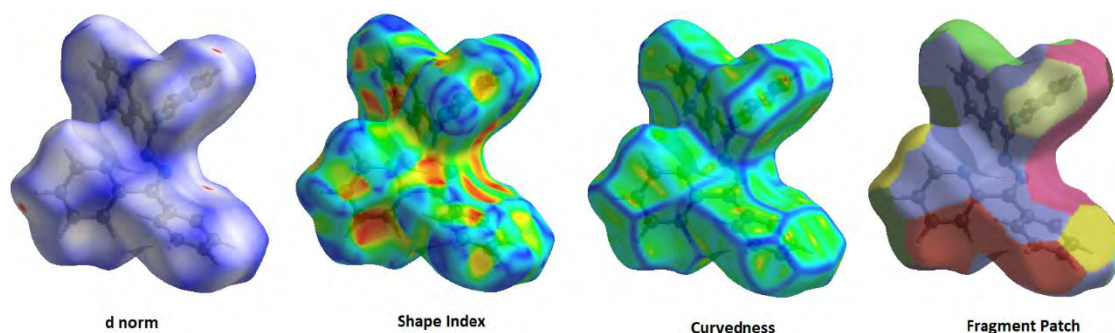


Fig. 3.13. Hirshfeld surface of L^2

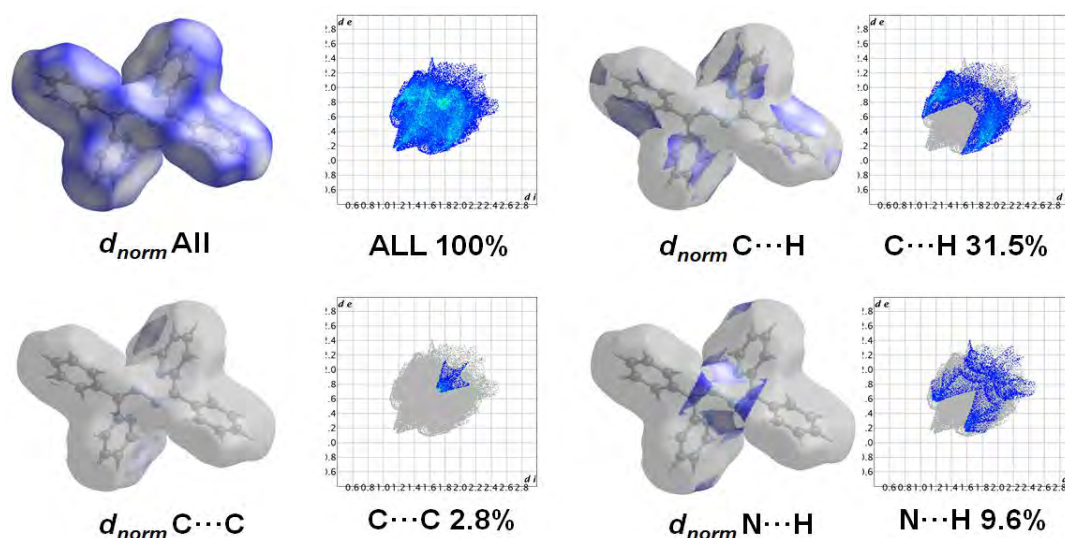


Fig. 3.14. Finger print plot of L^2

Table 3.8. Elemental contribution in the construction of 2D finger print plot

Atom Position	% of Surface occupy
All-in All-out	100
All-in N-out	6.8
All-in C-out	16.2
All-in H-out	77.0
N-in All-out	7.6
C-in All-out	21.4
H-in All-out	71.0

The energy framework analysis was computed on Crystal Explorer 21.2 software (Turner et al., 2017, Mackenzie et al., 2017) with HF/3-21G basis sets using TONTO software for the cluster environment of 3.8 Å surrounding a particular molecule of interest. The total interaction energy was articulated as $E_{tot} = k_{ele}E'_{ele} + k_{pol}E'_{pol} + k_{disp}E'_{disp} + k_{rep}E'_{rep}$, where the k values belong to the scale factors for benchmarked energy models. E'_{ele} represents the electrostatic energy, E'_{pol} represents the polarisation energy, E'_{disp} represents the dispersion energy, and E'_{rep} represents the repulsive energy (Table 3.9). To identify the type of interaction energies developed due to supramolecular interactions, we set the tube dimension factor 300 where a greater tube radius was directly proportional with stronger and more prominent interaction. From Fig. 3.15 it was clearly evident that the contribution of dispersive forces in total interaction energy was maximum over coulomb energy. These short-ranged dispersive forces account for isoenergetic and isotropic C-H $\cdots\pi$ and $\pi\cdots\pi$ interactions, thus played

a significant role in aggregation behaviour of L^2 . The predominance of dispersive forces was justified by the greater inner dimension of green cylinders than red cylinders between the same molecules. The total dispersive energy involved in the cluster of molecules was estimated to be -192.4kJ/mol.

Table 3.9. Energy framework analysis for L^2

	N	Symop	R	Electron Density	E_ele	E_pol	E_dis	E_rep	E_tot
	2	-x, -y, -z	7.78	HF/3-21G	-23.2	-8.0	-58.7	35.2	-53.3
	2	-x, -y, -z	10.44	HF/3-21G	0.7	-0.8	-10.2	4.7	-5.2
	2	x, y, z	5.58	HF/3-21G	-9.6	-7.6	-63.2	25.3	-51.1
	4	x+1/2, y+1/2, z	11.20	HF/3-21G	-4.6	-1.9	-29.5	17.2	-18.6
	2	-x, -y, -z	8.62	HF/3-21G	2.9	-1.3	-17.6	5.1	-9.6
	2	-x+1/2, -y+1/2, -z	12.94	HF/3-21G	-8.9	-1.0	-10.9	0.0	-19.5
	2	-x+1/2, -y+1/2, -z	14.56	HF/3-21G	0.6	-0.1	-2.3	0.0	-1.5

Energy Model	k_ele	k_pol	k_disp	k_rep
CE-HF ... HF/3-21G electron densities	1.019	0.651	0.901	0.811
CE-B3LYP ... B3LYP/6-31G(d,p) electron densities	1.057	0.740	0.871	0.618

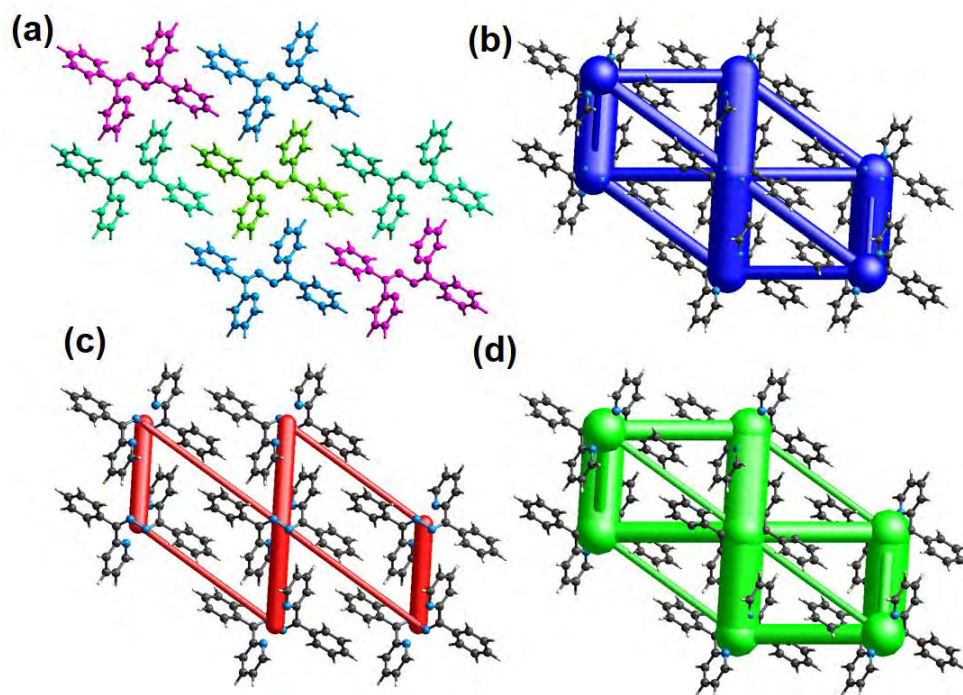


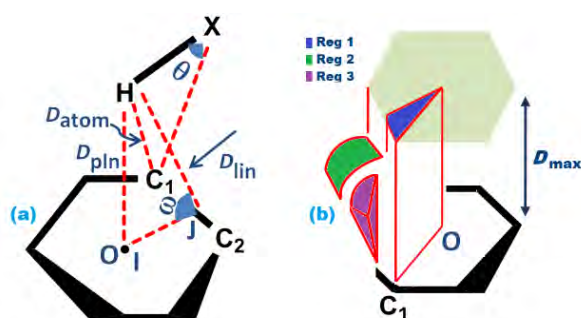
Fig. 3.15. (a) Energy framework diagram, (b) total energy plot, (c) coulomb energy contribution plot, and (d) dispersive energy contribution plot mapped for L^2 along b-axis

3.3.11. Structural perspectives and underlying mechanism for AIE property of the L^2

To decipher the role of weak forces for the assembled polarised or non-polarised aromatic molecules in supramolecular organic frameworks, we explored the propensity of dispersive energy for intermolecular C–H \cdots π and $\pi\cdots\pi$ interactions in the clusterisation of L^2 . Interesting, Martinez et al.^[49] attributed a valuable insight for the driving force in the association of polarised/non-polarised aromatic molecules through different proposals based on experimental observations and theoretical calculations such as the polar/ π model^[50], alternating e-rich and e-deficient aromatic- π interactions^[51,52], propensity of heteroaromatic π -systems^[53] and a large contact surface of π -electrons.^[54] The synthetic Schiff base contains flat and robust type phenyl and pyridine rings with a relatively large contact surface that might enable the dispersion force-induced stabilisation of the molecular aggregate as proposed by Martinez et al.^[53] However, flexible conformation with twisted orientations of aromatic rings facilitates the steric hindrance among the neighbouring aromatic rings, leading to a long distant face-to-face

aromatic interaction.^[55] It was scientifically evident that considerable intermolecular C–H... π interactions, also known as edge-to-face^[56], T-shaped^[57], can stabilise the crystal packing through restricted rotational orientations of the aromatic rings and make a pronounced effect on the molecular properties. Nishio and co-workers envisioned a significant effort to obtain valuable insights into the nature of C–H... π interactions.^[21,58] They reported that orientations of aromatic rings causing C–H... π interactions have a significant contribution in molecular packing and self-assembly.

It was a well-established fact that the charge transfer of π -e to the anti-bonding orbital of C–H bond principally account for the origin of C–H... π interactions.^[59,60] Nishio et al., surveyed the C–H... π interactions for 6-membered π -electronic systems varying the positions of hydrogen atoms on a π -plane^[58] (**Scheme 3.3**), where D_{pln} , D_{lin} and D_{atm} define the H... π (plane), H...(C₁C₂ line) and H...C₁ distances, respectively. The dihedral angles between the π -plane and HC₁C₂ plane as $\angle\text{HXC}_1$ angle (X= C,O, etc.) were represented as ω and θ , respectively. This model was applied by considering H... π distances shorter than a cut-off D_{max} value and $D_{\text{pln}} < D_{\text{max}}$, $\theta < 60^\circ$, $|\omega| < 90^\circ$ for **region 1**; $D_{\text{lin}} < D_{\text{max}}$, $\theta < 60^\circ$, $90^\circ < |\omega| < 130^\circ$ for **region 2**; $D_{\text{atm}} < D_{\text{max}}$, $\theta < 60^\circ$, $50^\circ < \phi < 90^\circ$ for **region 3** ($\phi = \text{HC}_1\text{I}$).



Scheme 3.3. C–H... π surveying model; a) O was the centre of the plane, C₁ and C₂ nearest and second nearest sp²-C to H, ω is the dihedral angle, $\angle\text{C}_1\text{OC}_2$ and $\angle\text{HC}_1\text{C}_2$, θ is $\angle\text{HXC}_1$; b) Region: Reg1, H is above on π -aromatic, Reg2 and Reg3 indicates H was out of the aromatic ring but may interact with π -electrons

This method was advantageous to validate the C–H...Ar contacts, and it is revealed that higher acidic-H would give rise to shorter mean values of H... π distances and the D_{pln} , and D_{atm} would also produce smaller values. They obtained the mean H... π distance for aromatic- C–H... π aromatic interaction as $2.76 \pm 0.10 \text{ \AA}$ for a 32282 number of CH...Ar

contacts. [58] Previously, Alvarez reported an interesting work for intermolecular contacts showed distance distribution maps between an element and a probe element, X, mostly oxygen. [61] The author summarised that most elements reserve a different distance in the distribution and provide a clear depiction between bonded and non-bonded atom pairs. [61] We also attempted to validate and examine the propensity of C–H... π interactions for L^2 and tetraphenylethene (TPE) following the method of Nishio et al. The measurement of D_{pln} , D_{lin} , θ and ω was well corroborated between L^2 and TPE (Table 3.10).

Table 3.10. Surveying of C–H... π interactions in L^2 and TPE through Nishio’s method

Aromatic rings with atom labels	D_{pln} , C–H... π	D_{lin} , H...(C ₁ C ₂ line)	θ , $\angle\text{HXC}_1$ C ₁ (nearest sp ² -C to H)	ω , $\angle\text{C}_1\text{OC}_2$ and $\angle\text{HC}_1\text{C}_2$	>/< vdW distances for H & sp ² -C (2.9Å)
C1C2C3C4C5N1 (Cg1)	C3H3... π (Cg2), 3.18 Å	H3...(C ₈ C ₇ line), 3.22Å	$\angle\text{H3–C3–C8}$ (Cg2) = 45.07°	$\angle\text{C8–C}_g(2)\text{–C7}$ = 59.64° $\angle\text{H3–C8–C7}$ = 80.86°	>vdW distances
C7C8C9C10C11C12 (Cg2)	C9–H9... π (Cg2), 2.93 Å	H9...(C ₈ C ₉ line), 3.12Å	$\angle\text{H9–C9–C8}$ (Cg2) = 43.68°	$\angle\text{C8–C}_g(2)\text{–C9}$ = 59.92° $\angle\text{H9–C8–C7}$ = 82.91°	>vdW distances
C1C12C20C21C22C23 (Cg1-TPE)	C16–H12... π (Cg1), 2.76 Å	H12...(C ₁ C ₁₂ line), 3.02Å	$\angle\text{H12–C16–C1}$ (Cg1) = 42.98°	$\angle\text{C1–C}_g(1)\text{–C12}$ = 59.81° $\angle\text{H–C8–C7}$ = 76.98°	<vdW distances
C1C12C20C21C22C23 (Cg2-TPE)	C3–H2... π (Cg2), 2.93 Å	H2...(C ₁ C ₁₂ line), 3.06Å	$\angle\text{H2–C3–C1}$ (Cg2) = 59.81°	$\angle\text{C1–C}_g(2)\text{–C12}$ = 59.81°	>vdW distances

			40.17°	∠H2– C1–C12 = 85.25°	
--	--	--	--------	----------------------------	--

Furthermore, the underlying principle of the AIE properties for this Schiff base was unveiled by comparing the structural characteristics of a widely studied tetraphenylethene (TPE) which exhibited a pronounced AIE phenomenon with the synthetic **L**². TPE was a nearly planar non-emissive molecule (**Fig. 3.16**) in solution because the excited-state energy of TPE dissipates through the free-rotations of the four phenyl rings attached to ethylene-C.^[2,62,63] However, intermolecular interactions restrict the intramolecular movement of the phenyl rings in the aggregated state and enable them to emit bright light.^[2,62,63] It was well established that TPE locked the phenyl rings in aggregated form based on restriction of intramolecular rotation (RIR) and vibrations (RIV), leading to an intriguing turn-on of fluorescence properties in molecular aggregates.^[62,63] The X-ray crystal structure of TPE was previously reported by Hoekstra et al.^[64], and we downloaded the deposited CIF from Cambridge Structural Database (CCDC 1275289) to compare structural features and C–H··· π contribution in the construction of supramolecular frameworks. **Fig. 3.16 (a,b,c,d)** displayed a combination of crystal structure, structure with selected bond distances and angles and interaction mapping of TPE which displayed close structural characteristics of **L**². Further, TPE showed two different short-ranged C–H··· π interactions (2.76 Å & 2.91 Å) while **L**² showed one short C–H··· π interactions (2.94 Å) with one distant (3.18 Å) C–H··· π interactions (**Fig. 3.17**). Both the compounds exist in nearly planar structures and exhibited a similar propensity for hydrophobic interactions (**Fig. 3.16-b,c,d**).

I also considered a previously reported azine compound, salicylaldehyde azine (SAA), comparing AIE properties with **L**². Typically, SAA adopts complete planarity due to its strong intramolecular hydrogen bonding interaction; however, the complete planarity of **L**² molecule cannot be achieved without any intramolecular H-bonding. SAA exhibited excited-state intramolecular proton transfer (ESIPT) and AIE characteristics.^[65,66] AIE and ESIPT processes were entirely different, although both were mutually compatible to turn on the fluorescence property of the molecules. The AIE property stems from RIR and RIM characteristics leading to emission enhancement, while ESIPT facilitated by excited-state proton transfer and consequent causing of significant Stokes shift with bright emission. In contrast to SAA, the

synthetic L^2 molecule displayed predominance short C–H $\cdots\pi$ interactions. Therefore, based on a spectroscopic, photophysical and details studied on self-assembly, energy framework analysis, it was recommended that interlocking of head-to-tail type of aromatic rings through dominant C–H $\cdots\pi$ short contacts lead to the nano-dimension aggregation with intense blue light emission.

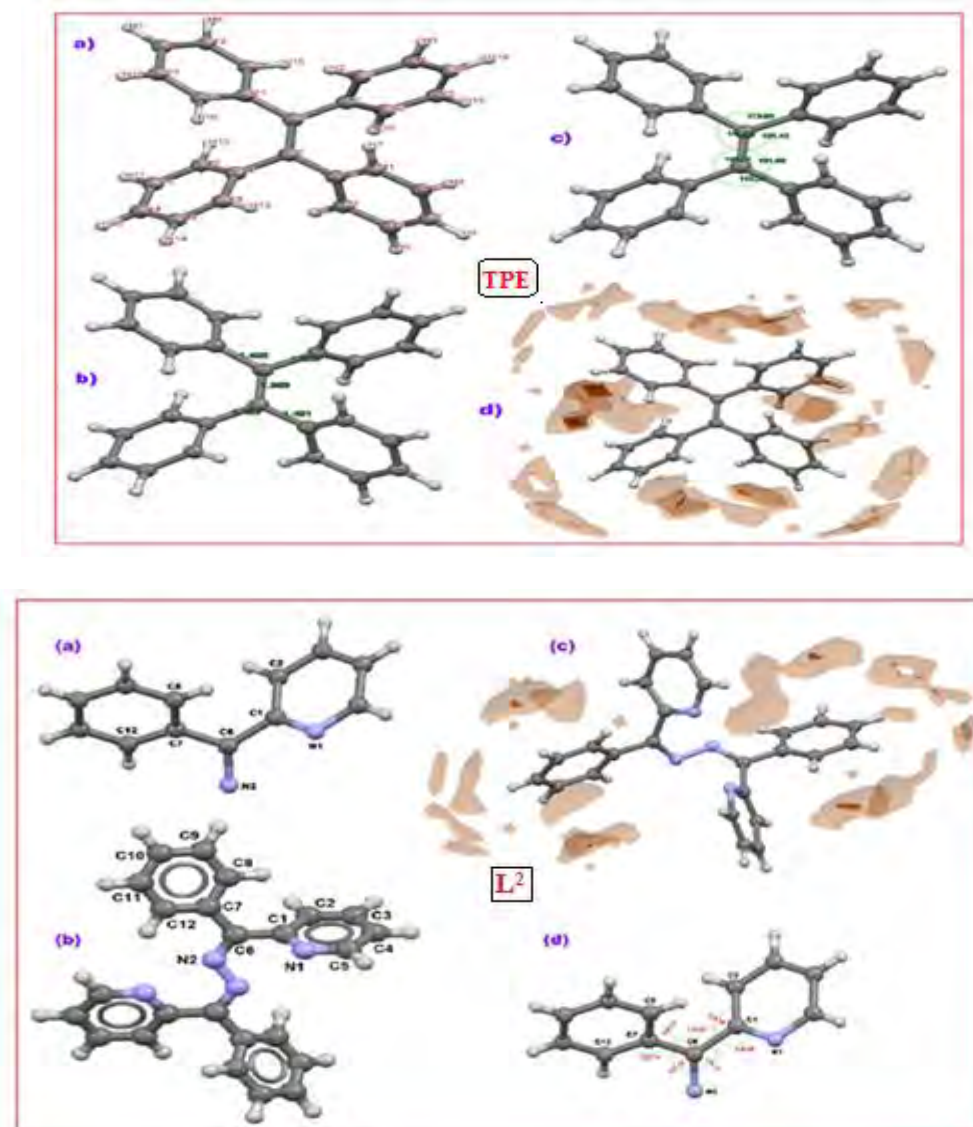


Fig. 3.16. (a,b,c,d) displayed a comparison of structural characteristics (crystal structure, structure with selected bond distances and angles and interaction mapping) between tetraphenylehene (TPE) and L^2

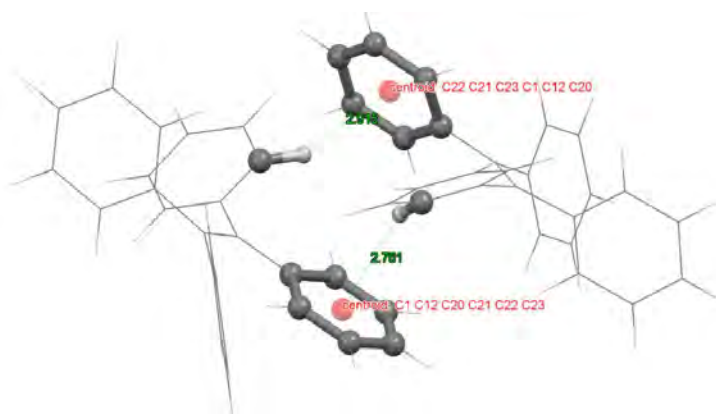


Fig. 3.17. C–H... π mediated dimer of TPE in crystalline state

3.4. Conclusions

In this present work, the aggregation behavior of a newly designed hydrazine functionalized Schiff base, L^2 was studied with a suite of spectroscopic, photophysical, and crystallographic methods. The structure of L^2 was well established with X-ray structure and found as *Z*-type stereomer in crystalline phase. A study on self-assembled structure suggests that there are no intermolecular H-bonding interactions in L^2 , although substantiate C–H... π and π ... π interactions among the neighbouring L^2 units helped to propagate the Schiff base in 3D. The interlocking of aromatic centroids through C–H... π and π ... π interactions provide an idea to measure the effect of C–H... π and π ... π interactions on the aggregation behaviour of L^2 . The aggregates of L^2 were developed employing the reprecipitation method without any external stabilizer. Interestingly, L^2 nano-aggregate exhibits a red-shifted absorption band as compared to L^2 in its molecular form. These spectral data was a definite signature for the formation of J aggregates for L^2 . The nano-aggregation displayed \sim 10-fold higher fluorescence intensity than that of molecular form of L^2 and exhibited a life time span \sim 1.09 ns. Furthermore, DLS studied of L^2 in aqueous medium suggested the hydrodynamic size \sim 270 nm. FESEM microscopy images with EDX spectrum strongly recommend the formation of \sim 250 nm aggregate through well characterized rectangular shaped nanodimensional L^2 . Principally, the head-to-tail type of interlocking among the aromatic centroids restricted the intramolecular motion as well as the rotational probability of =N–N= bond in L^2 drives to develop nano dimensional aggregate of L^2 .

References

- [1]. C. Zhu, R. T. K. Kwok, J. W. Y. Lam and B. Z. Tang, *ACS Appl. Bio Mater.*, 2018, **1**, 1768.
- [2]. Y. Chen, J. W. Y. Lam, R. T. K. Kwok, B. Liu and B. Z. Tang, *Mater. Horiz.*, 2019, **6**, 428- 433.
- [3]. Z. Zhao, H. Zhang, J. W. Y. Lam and B. Z. Tang, *Angew. Chem.*, 2020, **59**, 9888-9907,
- [4]. Y. Huang, J. Xing, Q. Gong, L. C. Chen, G. Liu, C. Yao, Z. Wang, H. L. Zhang, Z. Chen and Q. Zhang, *Nat. Commun.*, 2019, **10**, 169.
- [5]. D. Liu, K. Sun, G. Zhao, J. Wei, J. Duan, M. Xia, W. Jiang and Y. Sun, *J. Mater. Chem.*, 2019, **7**, 11005-11013.
- [6]. O. D. Parashchuk, A. A. Mannanov, V. G. Konstantinov, D. I. Dominskiy, N. M. Surin, O. V. Borshchev, S. A. Ponomarenko, M. S. Pshenichnikov and D. Y. Paraschuk, *Adv. Funct. Mater.*, 2018, **28**, 1800116.
- [7]. S. Kagatkar and D. Sunil, *J. Mol. Liq.*, 2019, **292**, 111371.
- [8]. J. Luo, Z. Xie, J. W. Y. Lam, L. Cheng, H. Chen, C. Qiu, H. S. Kwok, X. Zhan, Y. Liu, D. Zhu and B. Z. Tang, *Chem. Commun.*, 2001, 1740-1741.
- [9]. J. Chen, C. C. W. Law, J. W. Y. Lam, Y. Dong, S. M. F. Lo, I. D. Williams, D. Zhu and B. Z. Tang, *Chem. Mater.*, 2003, **15**, 1535-1546.
- [10]. Z. Zhao, X. Zheng, L. Du, Y. Xiong, W. He, X. Gao, C. Li, Y. Liu, B. Xu, J. Zhang, F. Song, Y. Yu, X. Zhao, Y. Cai, X. He, R. T. K. Kwok, J. W. Y. Lam, X. Huang, D. Lee Phillips, H. Wang and B. Z. Tang, *Nat. Commun.*, 2019, **10**, 2952.
- [11]. G. Yui, S. Yin, Y. Liu, J. Chen, X. Xu, X. Sun, D. Ma, X. Zhan, Q. Peng, Z. Shuai, B. Tang, D. Zhu, W. Fang and Y. Luo, *J. Am. Chem. Soc.*, 2005, **127**, 6335–6346.
- [12]. Z. Li, Y. Dong, B. Mi, Y. Tang, M. Häussler, H. Tong, Y. Dong, J. W. Y. Lam, Y. Ren, H. H. Y. Sung, K. S. Wong, P. Gao, I. D. Williams, H. S. Kwok and B. Z. Tang, *J. Phys. Chem.*, 2005, **B 109**, 10061–10066.
- [13]. C. W. Chang, C. J. Bhongale, C. S. Lee, W. K. Huang, C. S. Hsu and E. W. G. Diau, *J. Phys. Chem.*, 2012, **C 116**, 15146–15154.
- [14]. F. Wang, M. Y. Han, K. Y. Mya, Y. Wang and Y. H. Lai, *J. Am. Chem. Soc.*, 2005, **127**, 10350–10355.
- [15]. S. A. Jenekhe and J. A. Osaheni, *Science*, 1994, **265**, 765–768.

- [16]. R. H. Friend, R. W. Gymer, A. B. Holmes, J. H. Burroughes, R. N. Marks, C. Taliani, D. D. C. Bradley, M. Lo, W. R. Salaneck, D. A. D. Santos and J. L. Bre, *Nature*, 1999, **397**, 123–128.
- [17]. D. Oelkrug, A. Tompert, H. Egelhaaf, M. Hanack, E. Steinhuber, M. Hohloch, H. Meier and U. Stalmach, *Synth. Met.*, 1996, **83**, 231.
- [18]. B. K. An, J. Gierschner and S. Y. Park, *Acc. Chem. Res.*, 2012, **45**, 544.
- [19]. R. Taylor and O. Kennard, *J. Am. Chem. Soc.*, 1982, **104**, 5063–5070.
- [20]. G. R. Desiraju, *Acc. Chem. Res.*, 2002, **35**, 565–573.
- [21]. M. Nishio, *Cryst. Eng. Comm.*, 2004, **6**, 130–158.
- [22]. S. Mukherjee, S. Roy, S. Mukherjee and B. Biswas, *J. Mol. Struct.*, 2020, **1217**, 128348.
- [23]. G. R. Desiraju, *Curr Opin Solid State Mater Sci.*, 1997, **2**, 451-454.
- [24]. B. Chowdhury, M. Karar, S. Paul, M. Joshi, A. R. Choudhury and B. Biswas, *Sensors & Actuators B: Chemical*, 2018, **276**, 560-566.
- [25]. S. Alvarez, *Dalton Trans.*, 2013, **42**, 8617.
- [26]. D. Dey, A. Basu Roy, C.-Y. Shen, H.-L. Tsai, A. Ranjani, L. Gayathri, S. Chandraleka, D. Dhanasekaran, M. A. Akbarsha, N. Kole and B. Biswas, *J. Chem. Sci.*, 2015, **127**, 649-661.
- [27]. B. Olenyuk, J. A. Whiteford, A. Fechtenkotter and P. J. Stang, *Nature*, 1999, **398**, 796-799.
- [28]. X. Huang, Y. Jeong, B. K. Moon, L. Zhang, D. H. Kang and I. Kim, *Langmuir*, 2013, **29**, 3223–3233.
- [29]. S. Das, A. Sahu, M. Joshi, S. Paul, M. Shit, A. R. Choudhury and B. Biswas, *ChemistrySelect*, 2018, **3**, 10774-10781.
- [30]. P. K. Mudi, N. Bandopadhyay, M. Joshi, M. Shit, S. Paul, A. R Choudhury and B. Biswas, *Inorg. Chim. Acta.*, 2020, **505**, 119468.
- [31]. S. Roy, P. Paul, M. Karar, M. Joshi, S. Paul, A. R Choudhury and B. Biswas, *J. Mol. Liq.*, 2021, 115293.
- [32]. S. Mahato, N. Meheta, M. Kotakonda, M. Joshi, P. Ghosh, M. Shit, A. R Choudhury and B. Biswas, *Appl. Organomet. Chem.*, 2020, **34**, e5935.
- [33]. CrysAlisPro 1.171.39.35c, 2017, Rigaku Oxford Diffraction, Rigaku Corporation: Tokyo, Japan.
- [34]. G. M. Sheldrick, *Acta Cryst.*, 2015, **A71**, 3-8.
- [35]. G. M. Sheldrick, *Acta Cryst.*, 2015, **C71**, 3-8.

- [36]. O. V. Dolomanov, L. J. Bourhis, R. J. Gildea, J. A. K. Howard and H. Puschmann, *J. Appl. Cryst.*, 2009, **42**, 339-341.
- [37]. M. J. Turner, J. J. McKinnon, S. K. Wolff, D. J. Grimwood, P. R. Spackman, D. Jayatilaka and M. A. Spackman, *Crystal Explorer*, 2017.
- [38]. M. A. Spackman and D. Jayatilaka, *Cryst. Eng. Comm.*, 2009, **11**, 19.
- [39]. M. A. Spackman and J. J. McKinnon, *Crys.t Eng. Comm.*, 2002, **4**, 378.
- [40]. S. Pal, B. Chowdhury, M. Patra, M. Maji and B. Biswas, *Spectrochim. Acta Part A: Mol. Biomol. Spectros.* 2015, **144**, 148–154.
- [41]. D. Dey, G. Kaur, M. Patra, A. R. Choudhury, N. Kole and B. Biswas, *Inorg. Chim. Acta.*, 2014, **421**, 335-341.
- [42]. J. Zhao, Z. Feng, D. Zhong, X. Yang, Y. Wu, G. Zhou and Z. Wu, *Chem. Mater.*, 2018, **30**, 929–946.
- [43]. C. K. Pal, S. Mahato, M. Joshi, S. Paul, A. R. Choudhury and B. Biswas, *Inorg. Chim. Acta.*, 2020, **506**, 119541.
- [44]. R. Wang, C. Hao, P. Li, N. G. Wei, J. Chen and J. Qiu, *Clusters J. Comput. Chem.*, 2010, **31**, 2157–2163.
- [45]. M. Kasha, H. R. Rawls and M. A. El-Bayoumi, *Pure Appl. Chem.* 1965, **11**, 371–392.
- [46]. A. Datta and S. K. Pati, *J. Chem. Phys.*, 2003, 118, 8420.
- [47]. P. K. Mudi, S. Pradhan, A. Sahu, D. Saha, B. Biswas, *J. Appl. Microbiol. Theory & Technology*, 2021, **2**, 18-28.
- [48]. M. Karar, P. Paul, B. Biswas, T. Majumdar and A. Mallick, *J. Chem. Phys.*, 2020, **152**, 075102.
- [49]. C. R. Martinez and B. L. Iverson, *Chem. Sci.*, 2012, **3**, 2191-2201.
- [50]. C. A. Hunter, *Trans. R. Soc. London, Ser.*, 1993, **345A**, 77–85.
- [51]. S. Nepogodiev, J. Stoddart, *Chem. Rev.*, 1998, **98**, 1959–1976.
- [52]. J. J. Reczek, K. R. Villazor, V. Lynch, T. M. Swager and B. L. Iverson, *J. Am. Chem. Soc.*, 2006, **128**, 7995–8002.
- [53]. I. E. Craven, M. R. Hesling, D. R. Laver, P. B. Lukins, G. L. D. Ritchie and J. Urbancich, *J. Phys. Chem.*, 1989, **93**, 627–631.
- [54]. J. C. Ma and D. A. Dougherty, *Chem. Rev.*, 1997, **97**, 1303–1324.
- [55]. J. Chen, C. C. W. Law, J. W. Y. Lam, Y. Dong, S. M. F. Lo, I. D. Williams, D. Zhu and B. Z. Tang, *Chem. Mater.*, 2003, **15**, 1535–1546.

- [56]. A.V. Muehldorf, D. van Engen, J. C. Warner and A. D. Hamilton, *J. Am. Chem. Soc.*, 1988, **110**, 6561–6562.
- [57]. J. Pawliszyn, M. M. Szczesniak and S. Scheiner, *J. Phys. Chem.*, 1984, **88**, 1726–1730.
- [58]. Y. Umezawa, S. Tsuboyama, K. Honda, J. Uzawa and M. Nisho, *Bull. Chem. Soc. Jpn.*, 1998, **71**, 1207-1213.
- [59]. T. Takagi, A. Tanaka, S. Matsuo, H. Maezaki, M. Tani, H. Fujiwara and Y. Sasaki, *J. Chem. Soc. Perkin Trans.*, 1987, **2**, 1015.
- [60]. M.-F. Fan, Z. Lin, J. E. McGrady and D. M. P. Mingos, *J. Chem. Soc. Perkin Trans.*, 1996, **2**, 563.
- [61]. S. Alvarez, *Dalton Trans.*, 2013, **42**, 8617-8636.
- [62]. N. L. C. Leung, N. Xie, W. Yuan, Y. Liu, Q. Wu, Q. Peng, Q. Miao, J. W. Y. Lam and B. Z. Tang, *Chem. Eur. J.*, 2014, **20**, 1 – 6.
- [63]. J. Shi, N. Chang, C. Li, J. Mei, C. Deng, X. Luo, Z. Liu, Z. Bo, Y.Q. Dong and T. B. Zhong, *Chem. Commun.*, 2012, **48**, 10675–10677.
- [64]. A. Hoekstra and A. Vos, Section B: Struct. Crystallogr. *Cryst. Chem.*, 1975, **31**, 1716.
- [65]. J. E. Kwon and S. Y. Park, *Adv. Mater.*, 2011, **23**, 3615–3642.
- [66]. Z. Xie, B. Yang, G. Cheng, L. Liu, F. He, F. Shen and Y. Ma, *Chem. Mater.*, 2005, **17**, 1287–1289.